JGR Atmospheres

RESEARCH ARTICLE
10.1029/2020JD033051

Near-Global CFC-11 Trends as Observed by Atmospheric Infrared Sounder From 2003 to 2018

Xiuhong Chen[1], Xianglei Huang[1], and L. Larrabee Strow[2]

[1]Department of Climate and Space Sciences and Engineering, University of Michigan, Ann Arbor, MI, USA, [2]Department of Physics, University of Maryland at Baltimore County, Baltimore, MD, USA

Key Points:
- CFC-11 long-term signals can be extracted from the nadir-viewed infrared sounders such as AIRS using a double differential method
- CFC-11 long-term trends over each 30° by 10° grid from 55°S to 55°N are estimated from the AIRS clear-sky radiances from 2003 to 2018
- The result suggested possible regional slowdowns of the CFC-11 trend since 2013

Correspondence to:
X. Chen,
xiuchen@umich.edu

Citation:
Chen, X., Huang, X., & Strow, L. L. (2020). Near-global CFC-11 trends as observed by atmospheric infrared sounder from 2003 to 2018. *Journal of Geophysical Research: Atmospheres*, *125*, e2020JD033051. https://doi.org/10.1029/2020JD033051

Received 5 MAY 2020
Accepted 8 OCT 2020
Accepted article online 31 OCT 2020

Abstract Recent studies have indicated a slowdown of the decline of CFC-11 concentration since 2012. Ground-based observations used in such studies have their limitations in terms of global coverage. Here we show that the CFC-11 time-varying behaviors can be seen by double differencing nadir-view, clear-sky brightness temperatures of four AIRS (Atmospheric Infrared Sounder) channels in an infrared CFC-11 absorption band. Assuming that CFC-11 is vertically well mixed through the troposphere, we retrieve CFC-11 surface concentration and its secular trend using such AIRS observations over the near globe (55°S to 55°N) from January 2003 to December 2018. The retrieved trends of CFC-11 at the 11 ground sites agree well with the trends derived from in situ measurements at those sites. Our results show that, from 55°S to 55°N, the CFC-11 trends from January 2003 to December 2012 are all negative, ranging from −2.5 to −1 ppt/year. The trends from January 2003 to December 2018 are less negative by as much as ~0.5–1 ppt/year over the Shandong peninsula, the Arabian Peninsula, and north India and Nepal area, and such differences in the trends are statistically significant. Factors other than the CFC-11 that can affect the retrievals and trends are also discussed. These findings can help us depict the near-global spatial distribution of the CFC-11 trends from 2003 to 2018. The analysis described here has the potential to be used with current and future hyperspectral sounders to help monitor the CFC-11 from space.

1. Introduction

Trichlorofluoromethane (CCl_3F, also called CFC-11), widely used as refrigerants and blowing agents for polyurethane foam insulation, is the second-largest contributor in the chlorofluorocarbons (CFCs) to the stratospheric ozone-depleting. It was included in the Montreal Protocol of 1987 and entered into force in 1989, which aims to protect the global stratospheric ozone layer (World Meteorological Organization (WMO), 2011). Thus, it is expected that the CFC-11 concentration would decline when its usage was started to be phased out. However, recent observational studies (Montzka et al., 2018; Prinn et al., 2018) showed that the decline of CFC-11 has slowed down by ~50% since 2012. Montzka et al. (2018) also found the observed slowdown was concurrent with a ~50% increase in the mean difference of observed CFC-11 between the Northern and Southern Hemispheres. Rigby et al. (2019) discovered an increase of CFC-11 emissions primarily around the northeastern provinces of Shandong and Hebei in China. Lin et al. (2019) reported findings from a field campaign carried out in 2017 that the CFC-11 concentration in southwestern and central China then was higher than the background measurements in East Asia and the northern hemisphere. All these discoveries were based on surface in situ observations, which cannot provide the global, or at least near-global, spatial patterns of the trends. Limb-view satellite observations have been used before to provide global distributions of stratospheric CFC-11 (e.g., Hoffmann et al., 2008; Minschwaner et al., 2013). The long-term trend of tropospheric CFC-11 as observed from space is rarely reported, which is largely due to two facts: (1) the challenge to obtain the CFC-11 from nadir-view IR observations due to overlapped absorptions from other greenhouse gases and clouds, and (2) few high-quality, stable long-term IR observations with sufficient spectral resolutions previously available for nadir-view retrievals of CFC-11 trends.

Chen and Huang (2014) applied a double differential method to Atmospheric Infrared Sounder (AIRS) observations to provide a fast retrieval of total column water vapor. The double differential method can remove the attenuations slowly varying with frequency, such as continuum absorption of water vapor and attenuations due to clouds or aerosols, but retain the contrasts resulted from individual absorption lines. CFC-11 has two IR absorption bands, one entirely within the ozone absorption band (i.e., 1,060–1,108 cm^{-1}) and the other between 830 and 860 cm^{-1}, i.e., in the mid-IR window region. The dominant

Table 1
Information About the 11 Sites Used in This Study

Data repository	Sites	Full name and country	Latitude (°)	Longitude (°)	Altitude (m)	Contributor	Calibration scale
HATS combined (Montzka et al., 2018).	MHD	Mace Head, Ireland	53.3	−9.9	42	NOAA	NOAA 2016
	THD	Trinidad Head, United States	41.1	−124.2	120		
	NWR	Niwot Ridge, United States	40.1	−105.6	3,523		
	KUM	Cape Kumukahi, United States	19.5	−154.8	39		
	MLO	Mauna Loa, United States	19.5	−155.6	3,433		
	SMO	American Samoa, United States	−14.2	−170.6	77		
	CGO	Cape Grim, Australia	−40.7	144.7	164		
WDCGG https://gaw.kishou.go.jp/	LEF	Park falls, United States	45.9	−90.3	868	NOAA	NOAA 2016
	HFM	Harvard Forest, United States	42.9	−72.3	340	NOAA	NOAA 2016
	RYO	Ryori, Japan	39.0	141.8	260	JMA	A gravimetrically prepared standard
	RPB	Ragged Poin, Barbados	13.2	−59.4	45	AGAGE[a]	SIO 05

Note. The in situ CFC-11 measurements at the first seven sites are from NOAA Halocarbons and other Atmospheric Trace Species (HATS) group and the rest four sites are from a data repository, the World Data Centre for Greenhouse Gases (WDCGG), archived and managed by the Japan Meteorological Agency under the Global Atmosphere Watch (GAW) program.
[a]AGAGE is advanced global atmospheric gases experiment science team.

clear-sky absorptions in 830–860 cm^{-1} come from water vapor continuum as well as several weak line absorptions; therefore, the double differential method has the potential to obtain CFC-11 information from this spectral region. Since CFC-11 is a well-mixed gas in the troposphere, its surface concentration is well correlated with its total column concentration (Brown et al., 2013; Minschwaner et al., 2013). Therefore, if the double differential method can retrieve CFC-11 total column concentration, it can be used to infer the surface concentration of CFC-11.

AIRS has been collecting data since September 2002 with a dense sampling pattern (3 million spectra per day) and superb radiometric calibration and stability (Aumann et al., 2019). More details of the AIRS instrument and its performance are depicted in section 2. By the end of 2018, 22 billion spectra have been collected by AIRS. Given this vast amount of data and the excellent instrument performances, even a subset of carefully selected AIRS radiances has the potential to reveal CFC-11 long-term trends. Therefore, a meaningful question to explore is whether near-global CFC-11 trends can be obtained by applying the double differential methods to the clear-sky AIRS spectra. In this study, we use collocated AIRS, CERES (Clouds and the Earth's Radiant Energy System), and MODIS (Moderate Resolution Imaging Spectroradiometer) observations to select a subset of clear-sky AIRS spectra from 2002 to 2018 (Chen et al., 2013; Huang et al., 2008, 2010, 2014). The use of only clear-sky AIRS spectra effectively avoids challenges and complexity involved in cloudy-sky retrievals.

The rest of this paper is organized as follows. Section 2 describes the data that we used, such as CFC-11 in situ measurements, collocated clear-sky AIRS observations, as well as the methodologies for simulations of synthetic clear-sky AIRS spectra and for the CFC-11 retrieval. Section 3 presents results from double differential methods applied to the AIRS radiances and the CFC-11 retrieval results. The CFC-11 trend analysis is performed in section 4. Factors that can affect the CFC-11 retrieval and trend analysis are discussed in section 5. Conclusions and further discussions are then given in section 6.

2. Data Sets and Methodologies

2.1. Monthly CFC-11 In Situ Measurements

Eleven sites with continuous observations of CFC-11 from 2003 to 2018 are used in the study, primarily for validating the double differencing method and the CFC-11 retrieval results. The relevant information of 11 sites is listed in Table 1. The first seven sites provide monthly mean combined CFC-11 mole fractions from different measurement programs within the Halocarbons and other Atmospheric Trace Species (HATS) group of the NOAA Earth System Research Laboratory (Montzka et al., 2018). The programs include automated onsite instrumentation with gas chromatography coupled with electron capture detection (GC-ECD), gas chromatography-mass spectrometry (GC-MS), and paired glass or stainless-steel flasks instrument. The GC-ECD and GC-MS in situ instruments measured multiple times per day while the flask measurements

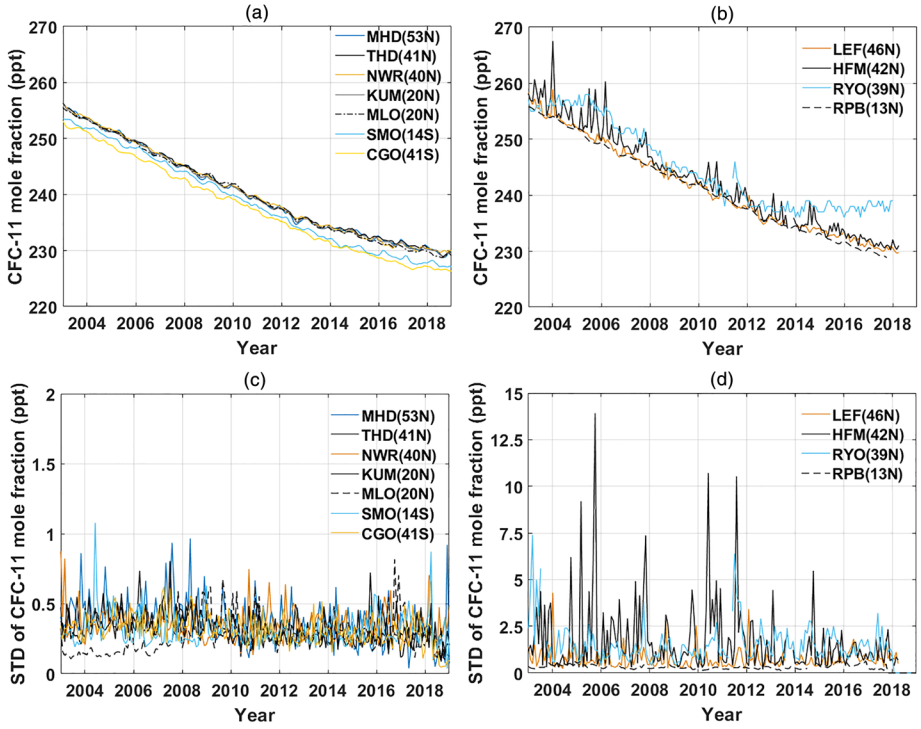

Figure 1. (a) Time series of monthly mean CFC-11 surface mole fraction (in ppt) for seven sites as measured by the NOAA Halocarbons and other Atmospheric Trace Species (HATS) group. (b) Same as (a) except for four sites from the World Data Centre for Greenhouse Gases (WDCGG) operated by the Japan Meteorological Agency. Panels (c) and (d) are same as (a) and (b) but for the standard deviation (STD) of the measured CFC-11 mole fraction within each month.

were collected weekly. The combined data are calculated by taking weighted averages of collocated measurements, and are calibrated on the same NOAA-2016 scale. The CFC-11 observations of the rest four sites are obtained from the World Data Centre for Greenhouse Gases (WDCGG), a data repository managed by the Japan Meteorological Agency (JMA) under the Global Atmosphere Watch (GAW) program (Japan Meteorological Agency and World Meteorological Organization, 2012). The four sites also used GC-ECD and GC-MS but reported CFC-11 concentration on different calibration scales. As shown in Table 1, CFC-11 concentration at the RPB and RYO sites was calibrated using SIO-05 scale and a gravimetrically prepared standard, respectively. Prinn et al. (2018) pointed out that differences between the NOAA-2016 and the SIO-05 scales are smaller than 1%. Therefore, such calibration scale difference will not affect the results discussed here. Figure 1 shows the monthly mean and standard deviation of the CFC-11 mole fractions obtained at the 11 sites.

2.2. Monthly Mean Gridded Nadir-View Clear-Sky AIRS Spectra

AIRS is a grating spectrometer aboard the NASA Aqua satellite, which is a sun-synchronous satellite with 1:30/13:30 (local time) equatorial crossing time. It measures 2,378 channels with a spectral resolving power ($\lambda/\Delta\lambda$) of 1,200 from 650 to 2,670 cm^{-1}, with several spectral gaps in between. AIRS is a cross-track scanning instrument with a viewing zenith angle no more than 49°. Its nadir field of view (FOV) at the surface is ~13.5 km. More details can be found in Aumann et al. (2003). It measures ~3 million spectra per day with global coverage in 1.5 days. Since September 2002, AIRS has collected more than 16 years of data (i.e., more than 20 billion spectra). The AIRS noise equivalent delta temperatures (NeDTs) at a scene temperature of 250 K are within 0.07–0.5 K over 650–2,665 cm^{-1} (Chahine et al., 2006; Pagano et al., 2003). AIRS has remarkable stability over the years. Aumann et al. (2006) estimated the stability to be better than 16 mK/year, and the estimate was updated to be ~4 mK/year by Aumann and Pagano (2008). Aumann et al. (2019) provided an updated estimation of the upper bound of AIRS radiometric stability, which is 2–3 mK/year. Such unprecedented calibration and stability performance, as well as the excellent global coverage, makes AIRS radiance ideal for trend studies.

In our study, clear-sky AIRS footprints are identified based on collocated clear-sky CERES Edition 4A footprints following procedures described in Huang et al. (2008) and Chen et al. (2013). Specifically, the time interval between the AIRS and CERES observations is less than 8 s, and the distance between the centers of their footprints is within 3 km. The collocated AIRS is deemed as a clear sky if the CERES FOV is deemed as a clear-sky FOV. A CERES FOV (~20 km at nadir view on the surface) is classified as a clear sky if there is no more than 0.1% cloud coverage in the FOV as inferred from the coincident MODIS pixels (Minnis et al., 2011). To avoid complexity with the viewing geometry in averages, we limited our data analysis for AIRS FOV within 5° viewing zenith angle. In this case, the AIRS FOV is guaranteed to be entirely within the CERES FOV. Moreover, given cos5° = 0.997, such AIRS FOV can all been deemed as nadir-view. All such clear-sky AIRS level 1B calibrated radiances (version 5) are then used in our study. For example, all such spectra in a given month can then be averaged onto 30° by 10° grids to form monthly time series of the AIRS radiances.

2.3. Synthetic Clear-Sky AIRS Spectra

When synthetic AIRS spectra are needed in this study, we use the temperature, water vapor, ozone profiles, and surface skin temperatures from European Center for Medium Range Weather Forecasting (ECMWF) ERA-Interim reanalysis (Dee et al., 2011) to generate such synthetic spectra. The 6-hourly ERA-Interim reanalysis is interpolated onto the same location and time as the individual AIRS observation and then used as input to a radiative transfer model, the MODerate resolution atmospheric TRANsmission computer code (MODTRAN5, Version 5). MODTRAN5 is based on the spectroscopy compilation of HITRAN 2008 (Rothman et al., 2009). The comparison with benchmark line-by-line calculation has shown satisfactory performance and computing efficiency (Anderson et al., 2007). It can simulate radiance at a spectral resolution up to 0.1 cm^{-1} with affordable computational efficiency.

To compute the synthetic AIRS spectra using MODTRAN5, the temperature, humidity, and ozone profiles from the surface to 1 hPa are from ERA-Interim reanalysis. Above 1 hPa, default standard profiles (McClatchey et al., 1972) are used. CO_2, CH_4, CO, and N_2O concentrations are from the standard atmospheric profiles compiled by McClatchey et al. (1972). Based on previous studies (Brown et al., 2013; Minschwaner et al., 2013), the satellite retrievals of CFC-11 vertical profiles show that CFC-11 concentrations are vertically uniform from the surface to a certain height (Z_0). The height Z_0 is ~22 km in the tropics and linearly decreases to 6 km at poles. At ~5 km above Z_0, the CFC-11 mole fraction decreases to zero. In our simulation, we assume the CFC-11 profiles have similar vertical and latitudinal distribution. With such assumptions, the entire profile can be scaled with the CFC-11 surface concentration. Surface types of the 11 ground-observation sites are determined based on their geographical location and the USGS International Geosphere-Biosphere Programme (IGBP) land coverage data set (Loveland et al., 2000). Once the surface type is decided, the corresponding surface spectral emissivities are then taken from the Advanced Spaceborne Thermal Emission Reflection Radiometer (ASTER) Spectral Library version 2.0 (Baldridge et al., 2009). The MODTRAN5 output at a spectral resolution of 0.1 cm^{-1} is convoluted with the spectral response function of an individual AIRS channel (Strow et al., 2006) to produce the synthetic AIRS radiance at the same channel.

2.4. Using the Double Differential Method for the CFC-11 Retrieval

Figure 2a illustrates the double differential method used in this study. From 830 to 860 cm^{-1}, major clear-sky absorptions are H_2O lines, H_2O continuum, and CFC-11 lines. The absorptions by CO_2, O_3, N_2O, CO, CH_4, CFC-12, CFC-113, and HCFC-22 are all nearly zero within this spectral range. Two pairs of AIRS channels, denoted as (A, B) and (C, D), reside away from the centers of H_2O absorption lines. The water vapor continuum absorption can be deemed as linearly varying with frequency within this spectral range. Therefore, when the spectral interval between A and B equals that between C and D, the effect of H_2O continuum absorption can be largely canceled by taking the double difference of $(BT_D\text{-}BT_C) - (BT_B\text{-}BT_A)$ where BT denotes the brightness temperature of the given channel. Meanwhile, because channels B and C sit around the center of the CFC-11 band while channels A and D are at the wing of the CFC-11 band, the center-to-wing absorption difference (orange dash-dotted line in Figure 2a) are amplified by such double differencing. As a result, the double difference clearly reveals the absorption due to CFC-11. After carefully evaluating individual channel performances over the years, we chose four AIRS channels listed in Table 2 to construct the double difference, hereafter denoted as dΔBT.

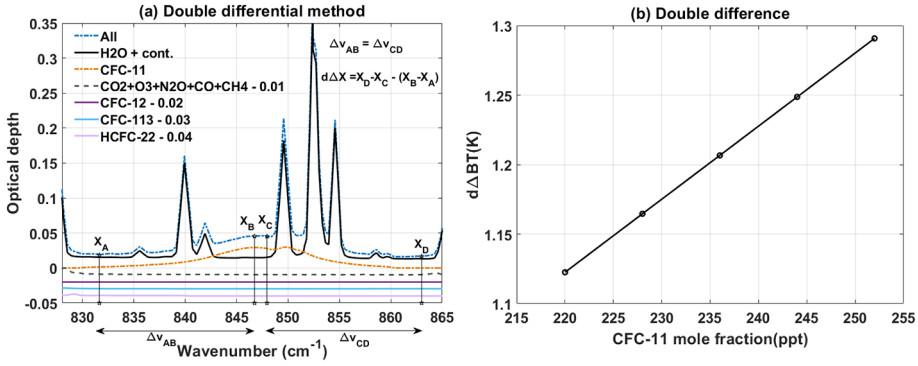

Figure 2. (a) Clear-sky optical depth at the surface due to all gases line and continuum absorptions (blue dash-dotted line), H_2O line and continuum absorption only (black line), CFC-11 only (orange dash-dotted line), $CO_2 + O_3 + N_2O + CO + CH_4$(black dashed line), CFC-12 only (purple solid line), CFC-113 only (cyan solid line), and HCFC-22 only (light violet solid line), the last four of which shift each by −0.01 for visual clarity (they are all flat to zero). Concentrations of H_2O, CO_2, O_3, N_2O, CO, and $CH_4$are from standard sub-Arctic winter profile (McClatchey et al., 1972). Mole fraction of all chlorofluorocarbons is set to be 274 ppt throughout the atmosphere. A–D denote four channels used for the double difference (Table 2). MODTRAN5 is used for this calculation. (b) Double difference of brightness temperature (dΔBTs) simulated for five different CFC-11 mole fractions. For illustration purpose, the standard tropical profile (McClatchey et al., 1972) is used in the simulation.

Once the dΔBT is obtained, we use a look-up-table (LUT) approach to retrieve CFC-11 surface concentration. Specifically, for any individual clear-sky footprint of AIRS collocated with CERES data within 60°S–60°N, five sets of synthetic AIRS spectra were produced. They are simulated using MODTRAN5, interpolated ECMWF ERA-Interim reanalysis profiles, and varying CFC-11 surface concentrations from 220 to 252 parts-per-trillion (ppt) with an increment of 8 ppt. By doing so, five dΔBTs can be obtained, corresponding to five different values of CFC-11 concentrations used in the calculation. For a given set of temperature and humidity profiles, there is a good linear relationship between the CFC-11 concentration and dΔBTs, as shown by an example in Figure 2b. To improve the signal-to-noise ratio, for each month, such LUT and the actual AIRS dΔBT of each individual clear-sky footprint are averaged onto a 30° longitude by 10° latitude grid and the CFC-11 surface concentration of the grid box is estimated from the corresponding LUT and averaged dΔBT. The number of clear-sky footprint within a month varies significantly from one grid box to another. To ensure enough samples for the long-term trend analysis, only grids with at least 30 clear-sky footprints are used for the CFC-11 retrieval and the subsequent linear trend analysis.

2.5. Retrieval Uncertainty Estimation

We perform bootstrap analysis to estimate the CFC-11 retrieval uncertainties following Conway et al. (1994), which used bootstrap analysis to estimate uncertainties in the NOAA CO_2 measurements. Specifically, let the retrieved CFC-11 concentration be expressed as,

$$\mathrm{CFC-11} = \mathrm{f}(\mathrm{d}\,\Delta\mathrm{BT}, \mathrm{LUT}), \tag{1}$$

where f denotes the relationship of CFC-11 concentration to dΔBT as tabulated in the LUT. Each month and each grid box, we derive CFC-11 concentration 100 times, each time using randomly selected half set

Table 2
The AIRS Spectral Channels Used in This Study and the Major Absorption Features in Each Channel

	Channel no.	Frequency (cm^{-1})	Major absorption features
A	556	831.6361	Weak water vapor continuum absorption
B	593	846.3286	Weak water vapor continuum absorption and CFC-11
C	597	847.9463	Weak water vapor continuum absorption and CFC-11
D	646	862.9984	Weak water vapor continuum absorption

Note. The double difference in BT, dΔBT, is computed as $(BT_D\text{-}BT_C) - (BT_B\text{-}BT_A)$.

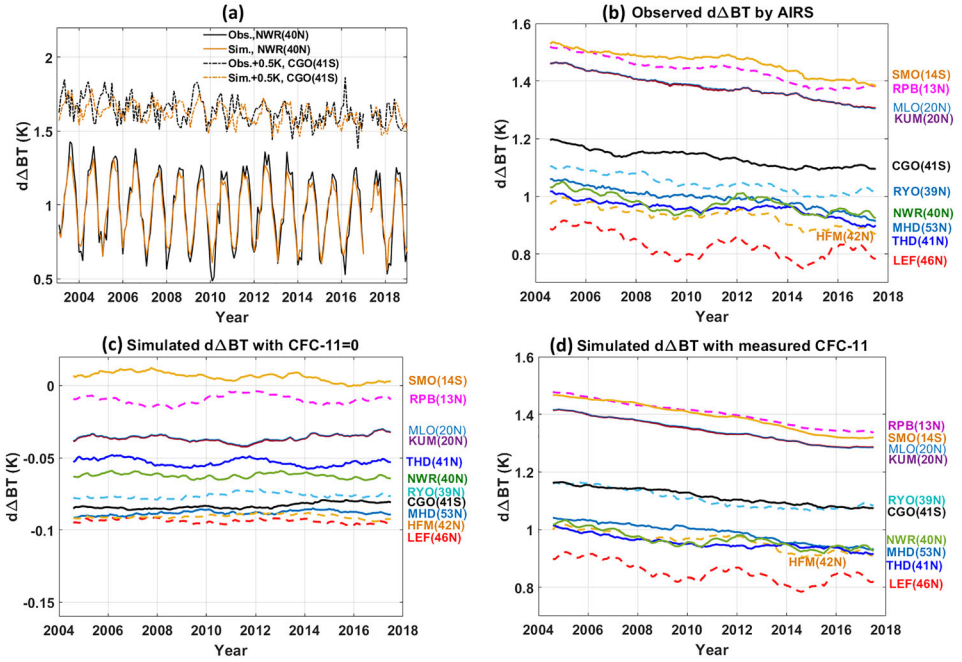

Figure 3. (a) Monthly mean time series of observed (black) and simulated (orange) double difference of brightness temperature (dΔBT) over the NWR site (solid lines) and the CGO site (dash-dotted lines; shifted by 0.5 K for better visualization. The simulation details can be found in section 2.3. (b) Time series of the observed dΔBTs from the clear-sky and nadir-view AIRS observations on the 30° by 10° grids that contains the 11 sites used in Figure 1. A 37-month running mean is used to better reveal the long-term behavior. (c) Same as (b) but from simulated monthly dΔBTs with CFC-11 being set to zero. (d) Same as (c) except for that the observed CFC-11 concentrations at the 11 sites are used, respectively. The measured CFC-11 mole fractions for the 11 sites are from Montzka et al. (2018) and from WDCGG. Site names are labeled in the order of lines on the right of each panel.

of all dΔBTs within the grid. The standard deviation of such 100 estimations is then deemed as the uncertainty for the retrieval. We note here that the uncertainty associated with the LUT retrieval approach can be estimated in other ways as well (e.g., Western et al., 2020).

3. Results

3.1. Comparison Between the Simulated and Observed dΔBTs

Figure 3a shows the observed AIRS dΔBTs monthly mean time series over the NWR and the CGO sites as well as the simulated counterparts. The simulation is done with the ERA-Interim temperature and humidity fields as well as observed CFC-11 concentration from the in situ measurements at each site. The seasonal cycle is obvious at the both sites, and the simulated time series can closely track the observed ones. The time series of observed AIRS dΔBTs over the 11 surface observation sites is shown in Figure 3b, smoothed with a 37-month running mean for better visualization of the long-term trend (as the seasonal cycle over each site can be considerably different in magnitude and phase). Please note trends in the following discussion are always calculated from the original monthly mean time series, and the smoothed time series is only for better visualization here. The smoothed AIRS dΔBTs are positive and larger than 0.7 K for all 11 cases. The long-term trends are self-evident for all the time series.

For comparison, we carried out two sets of simulations over the 11 sites to generate synthetic AIRS spectra and simulated dΔBTs. CFC-11 concentration is set to zero in the first set and to the observed CFC-11 concentration by the respective site in the second set (the same as the simulated ones in Figure 3a). The simulated dΔBTs, smoothed by 37-month running mean, are shown in Figures 3c and 3d, for the first and second sets, respectively. When CFC-11 is set to be zero, the dΔBTs only vary between −0.1 and 0.02 K, and no long-term trend can be seen from any time series. When CFC-11 is set to be the in situ observed values, the dΔBTs vary in a much larger range, i.e., between 0.7 and 1.5 K, the same range as the observed AIRS dΔBTs. This

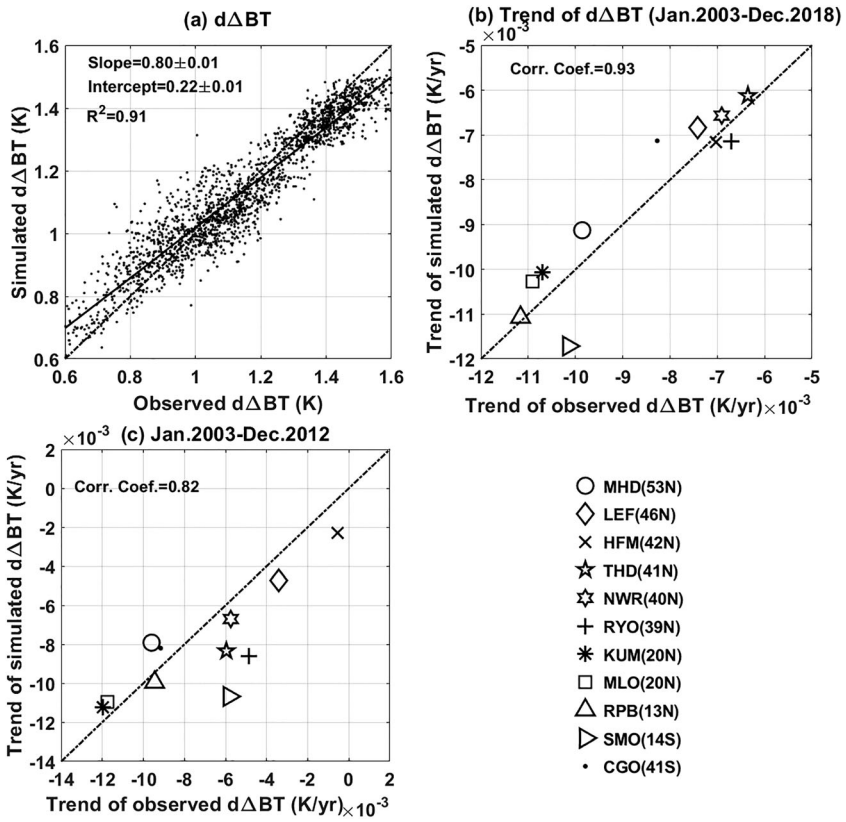

Figure 4. (a) Scatter plot of simulated versus observed monthly dΔBTs from January 2003 to December 2018 as shown in Figures 3b and 3d. Each dot denotes a site in a given month. The linear regression is shown in a solid black line, and the 1:1 reference line is shown in a dashed line. The regression slope, intercept, and R-square are summarized on the panel. (b) Scatter plot of the simulated versus observed trends of dΔBTs over the 11 sites for the period of 2003–2018. Each symbol denotes a site. The correlation coefficient is labeled on the panel. (c) Same as (b) but for the first 10-year period, i.e., 2003–2012.

confirms that, as articulated in subsection 2.4, the dΔBTs is indeed sensitive to the change of CFC-11. Moreover, the long-term trend is immediately visible in Figure 3d and largely agrees with the observed counterparts in Figure 3b.

When the observed and simulated monthly dΔBTs from January 2003 to December 2018 overall 11 sites are plotted on a scatterplot, they are highly correlated with each other with a linear correlation coefficient (r) of 0.95 (Figure 4a). The long-term trends of dΔBT over the same period as derived from the AIRS observation and from the synthetic spectra are plotted against each other in Figure 4b. The observed and simulated trends are also correlated well with $r = 0.93$. If we limit the period for the trend analysis to 2003–2012, the good correlation still holds ($r = 0.82$; Figure 4c). On both scatter plots, the site that deviates the most from the 1:1 line is SMO at 14°S, a site featured with a frequent pass of tropical convective systems, including detached anvil clouds. The frequent anvil cloud occurrences might be a challenge for the clear-sky detection (e.g., an AIRS FOV partly covered by subvisible thin cirrus might be deemed as a clear-sky FOV). Nevertheless, the overall good agreements between the observation and simulation strongly indicate that the CFC-11 signals are discernible from such dΔBTs.

3.2. Retrieved CFC-11 Trends Over the 11 Sites

Figure 5a shows the time series of retrieved CFC-11 surface concentrations at the aforementioned 11 sites, again smoothed by 37-month running mean. Compared to Figure 1a, the differences between retrieved CFC-11 time series and observed by ground observation are within ±10 ppt (i.e., ~ ± 4% relative

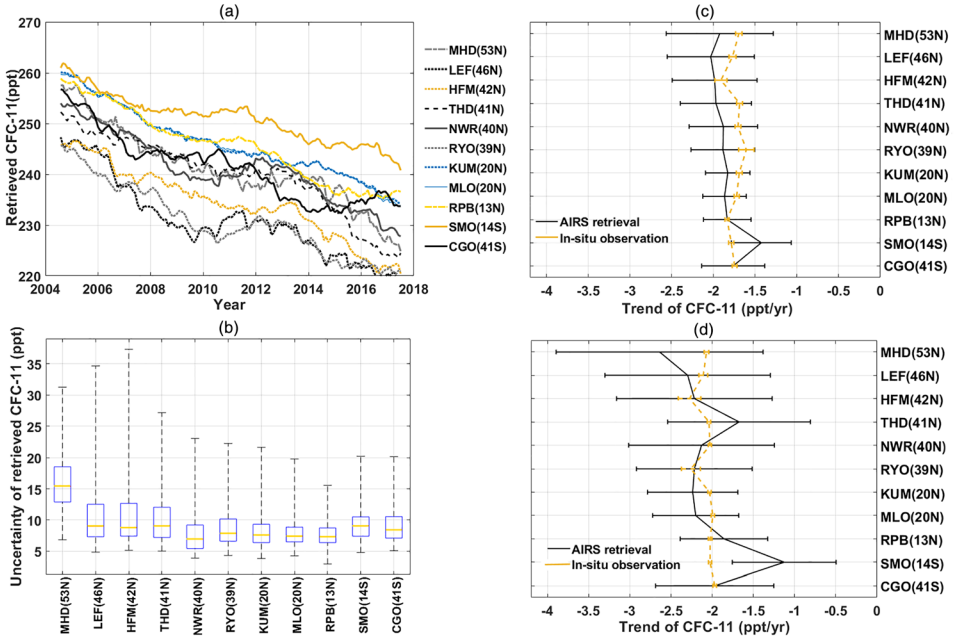

Figure 5. (a) Time series of monthly mean CFC-11 retrieved from AIRS observations for the grid boxes that contain the individual 11 sites. For better visualization, a 37-month running mean is applied. (b) Boxplot of the retrieval uncertainties for the 11 sites (see section 2.5for the method). The bottom and top edges of whiskers represent the minimum and maximum values, respectively. The yellow line indicates the median, and the bottom and top edges of the box are the 25th and 75th percentiles, respectively. (c) Trend of monthly mean CFC-11 from the AIRS retrieval in this study (black line) and from the NOAA HATS and WDCGG observations (yellow line), over the 11 sites, for the entire 16-year period (2003–2018). The horizontal ticked lines indicate the 95% confidence interval. (d) Same as (c) except for the period of 2003–2012.

difference). Since the focus here is the CFC-11 concentration trend instead of its absolute value, we did not do one-time calibrations for the retrievals as what has been done to the CO_2 retrievals using the AIRS radiances (Strow & Hannon, 2008). The calibration would be possible if we had a set of simultaneous independent observations of the CFC-11 column density when the AIRS observations were made over the same locations. The monthly retrieval uncertainties over each site are summarized in Figure 5b. Among 192 months studied here, the median retrieval uncertainty is no more than 10 ppt for all sites except one. Figure 5c shows the linear trends of surface-observed and satellite-retrieved CFC-11 concentrations at the 11 sites for 2003–2018. The surface measurements show a trend between −1.9 and −1.6 ppt/year, all within 95% confidence intervals of the trends estimated from CFC-11 retrievals in this study. With no surprise, the trends from the retrievals have a much larger confidence interval than their counterparts from the surface observations, due to the complexity and uncertainty associated with the retrievals. The largest difference between the retrieved and surface-observed CFC-11 trends is about 0.36 ppt/year at the SMO site, consistent with the dΔBT comparisons in Figure 4b. Similar conclusions can be drawn from the comparisons of linear trends derived from the first 10 years of CFC-11 concentrations (i.e., from 2003 to 2012), as shown in Figure 5d.

Multiple factors can contribute to the large uncertainties in retrieved CFC-11 trends. Uncertainty in clear-sky scene identification based on MODIS imageries can obviously affect the retrieval results. As we use the reanalysis profiles to construct the LUTs, the quality of ERA-Interim reanalysis, especially any time-dependent artifacts in the reanalysis, can also affect the retrieval and its trend. To increase the signal-to-noise ratio, we have to average 1 month of observations within a 30° by 10° grid. The sampling statistics are not the same for all grids, and the temperature and humidity are not uniform with such a large spatial grid box. All these can affect the retrieved trends and associated uncertainties. Nevertheless, Figure 5 shows reasonable agreements with the surface-observed trends over the 11 sites, which motivates us to further carry out the retrievals of CFC-11 over other grid boxes.

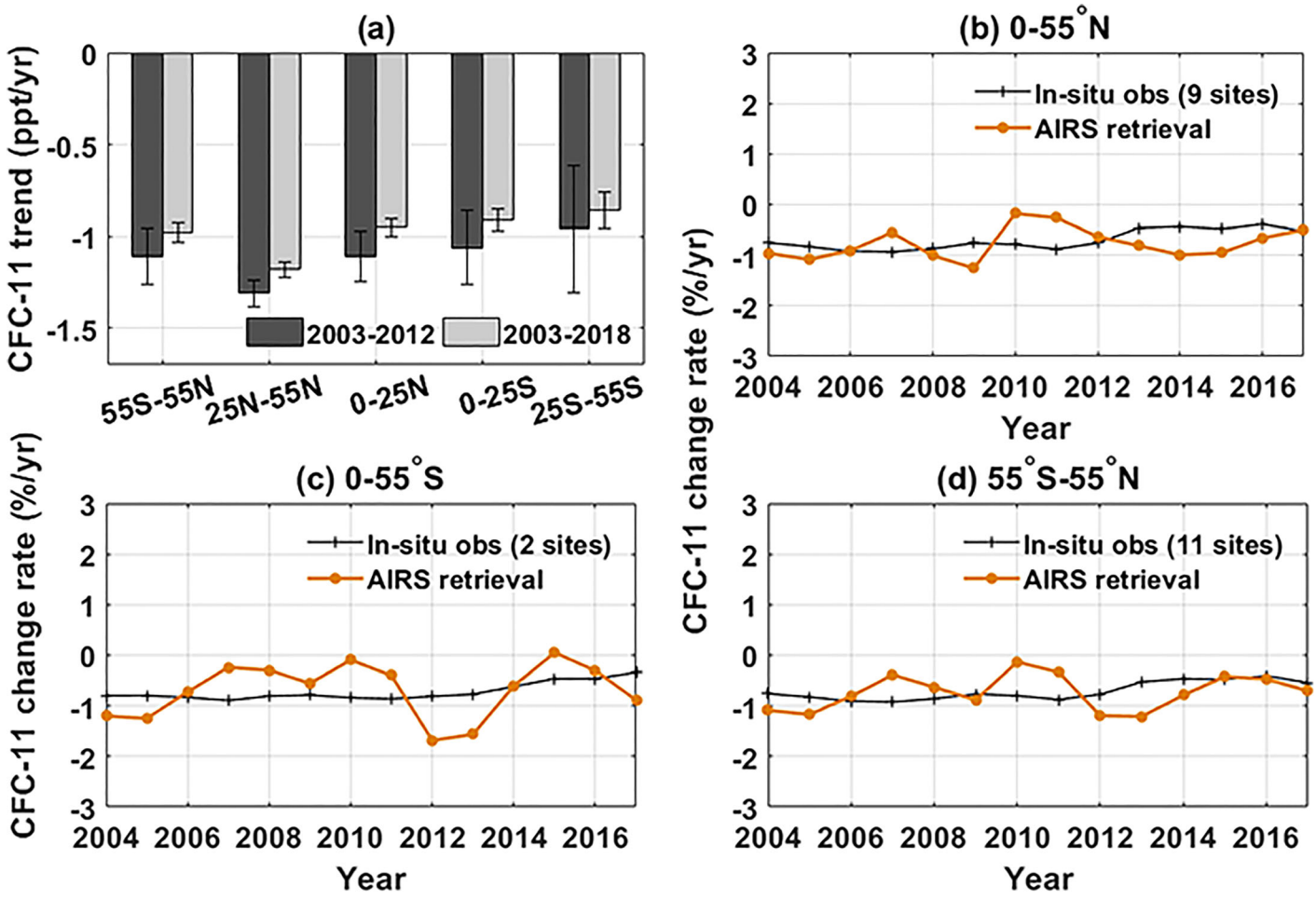

Figure 6. (a) CFC-11 linear trends in ppt/year over four climate zones and near globe, for the first 10 years (dark gray) and the entire 16 years (light gray). The vertical ticks indicate the 95% confidence interval. (b) Annual change rate of retrieved CFC-11 concentration averaged over 0–55°N (orange). For comparison, the estimated change rate from in situ measurements is shown in black (observations from each site weighted by the cosine of the latitude). (c) Same as (b) but for 0–55°S. (d) Same as (b) but for 55°S–55°N.

4. Near-Global Trend of Retrieved CFC-11 Surface Concentration

Given the quality of reanalysis in the polar region, we limit our effort here between 55°S and 55°N. Using the same retrieval algorithm, monthly CFC-11 surface concentration for each 30° longitude by 10° latitude grid is retrieved from the clear-sky AIRS observations, and then the secular trends are computed. As mentioned in section 2, linear trends are only computed for the grid boxes with enough clear-sky samplings each month.

4.1. Near Hemispheric and Global Growth Rate and Linear Trends in Different Climate Zones

Figure 6a shows the linear trends of the first 10-year period (2003 to 2012) and the entire 16-year period (2003 to 2018) for four climate zones (i.e., northern hemispheric tropics, midlatitude, and southern hemispheric tropics and midlatitude) and the entire domain from 55°S to 55°N. All four climate zones show a larger trend for the first 10 years than for the entire 16 years, suggesting a slowdown of the decrease of CFC-11 in the period of 2012–2018. If taking the 95% confidence interval into account, only the northern-hemispheric midlatitude zone has two trends separated from each other, further suggesting that the slowdown in this climate zone is statistically significant. The annual CFC-11 change rate over each near-hemisphere and the entire domain is calculated using the central differencing schemes and compared with the estimate from the in situ observations (i.e., nine sites in the northern hemisphere and two sites in the southern hemisphere), the results are shown in Figures 6b–6d. The retrieved annual change rate exhibits much larger year-to-year

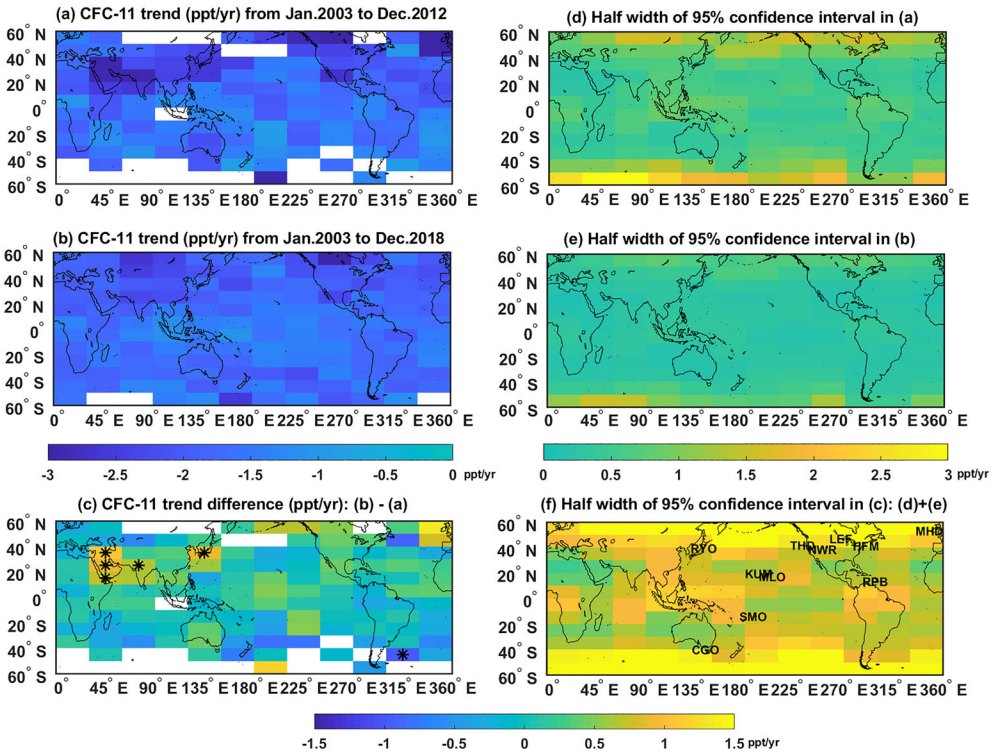

Figure 7. (a) Spatial map of CFC-11 trends in ppt/year as retrieved from the AIRS on 30° by 10° grids for the period of January 2003 to December 2012. Trends without enough statistical significance (5% significance level) are shown as blank. (b) Same as (a) but for the period of January 2003 to December 2018. (c) Difference between (b) and (a). Six grids marked with "*" have statistically significant difference between the 16-year trend and the 10-year trend. Panels (d) and (e) are the half width of 95% confidence intervals of the CFC-11 trends in (a) and (b), respectively. (f) Is the half width of 95% confidence intervals of CFC-11 trend difference, which is (d) + (e). The geographical locations of the 11 sites are labeled on (f).

variation than the in situ estimate. Such large fluctuation is highly likely resulted from retrieval uncertainties and artifacts: it is much more challenging to retrieve the change rate than to retrieve the CFC-11 concentration, as the former is a residual quantity of the latter.

4.2. Spatial Map of the Trends

Given the reasonably good agreement between satellite-retrieved and the surface-observed CFC-11 trends over the 11 sites, we further try to estimate the CFC-11 trend of each grid box. Figure 7a shows the linear trend over each grid at 5% significance level for the first 10-year period (2003–2012). The corresponding half width of the 95% confidence interval is shown in Figure 7d. All the trends are negative, ranging from approximately −1 to −2.5 ppt/year. The trends, still at 5% significance level, for the entire 16-year period (2003–2018) are shown in Figure 7b. Figure 7c shows the difference between the 16-year trend and the 10-year trend. A slowdown of negative trends (i.e., the trend difference in Figure 7c being positive) prevails the northern hemisphere midlatitude land area, but only five grid boxes show a statistically significant positive difference between the two trends. One grid box covers the Shandong peninsula with a slowdown of ~1 ppt/year, consistent with previous findings in Rigby et al. (2019). Of the remaining four grid boxes, three are located in the Arabian Peninsula with a slowdown of ~1 ppt/year and one across northern India, Pakistan, and Nepal with a slowdown of ~0.5 ppt/year. Coincidently, ground-based CFC-11 measurements from post-CFC11-phaseout campaigns have identified high CFC-11 concentrations over Mecca in Saudi Arabia, Lahore in Pakistan, and Kathmandu in Nepal (Simpson et al., 2019). Their ground measurement campaigns recorded CFC-11 as high as 620 ppt from garbage burning in Nepal in a 2015 campaign and 670 ppt from a landfill fire near Mecca in a 2013 campaign. Such coincidence might be worthy of future investigation. A grid box over the Southern Atlantic, close to Argentina's coastline, shows a statistically significant negative difference (Figure 7c). This is likely due to retrieval artifacts as

there has little evidence suggesting an acceleration of CFC-11 reduction after 2013, especially over the Southern Ocean.

5. Further Discussion of Uncertainties and Factors in the Retrieval and Trend Analysis

As shown in the previous two sections, the retrieval here has more substantial uncertainty than in situ measurements. Moreover, the method itself also has intrinsic limitations. Here we further examine several factors that can affect the retrieval and trend analysis.

1. AIRS radiometric calibration and stability: the noise equivalent brightness temperature for the AIRS channels used here is ~0.1 K (Pagano et al., 2003). The radiometric stability is estimated to be at ~2–3 mK/year (Aumann et al., 2019). The dΔBT caused by the CFC-11, as shown in Figures 3 and 4a, is ~0.8–1.6 K. Therefore, the impact of radiometric calibration and stability on the dΔBT and hence on the CFC-11 retrieval should be limited.
2. Surface spectral emissivity: surface emissivity can vary with frequency. Dependent on actual mineral compositions, the desert surface can exhibit a great variety of such spectral variations (Hulley et al., 2009). All the desert surface spectral emissivity measured in Hulley et al. (2009) exhibits monotonical decrease with frequency for the CFC-11 band studied here; thus, the double differential method can largely remove its contribution, in the same way as eliminating other slow-varying spectral components. The ASTER surface spectral emissivity used in our forward model has only one type of desert spectral emissivity. To further test the impact of surface spectral emissivity, we used a time-dependent surface emissivity data set, CAMEL (Combined ASTER MODIS Emissivity over Land; Borbas et al., 2018; Feltz et al., 2018), to redo the CFC-11 retrievals for a grid box over the Arabian Peninsula (30–40°N, 30–60°E). The CAMEL data set so far has only provided surface emissivity up to 2016. The CFC-11 retrievals derived in this way are highly consistent with those derived using our method. Moreover, unlike surface albedo, which can vary significantly from one surface type to another, the surface spectral emissivity in the band of 830–860 cm^{-1} is above 0.95 for all surface types except ice (Huang et al., 2016). The ice surface is largely excluded in our study, as the retrievals are limited between 55°S and 55°N. Therefore, even there is some land cover change, its impact on CFC-11 retrieval through the change of surface emissivity should be limited.
3. Uncertainties in the reanalysis temperature and humidity fields: since the temperature and humidity profiles from the ERA-Interim reanalysis is used in our LUT construction, any systematic biases in such reanalysis profiles can affect the retrievals. This is particularly true for temperature profiles as infrared remote sensing is relying on the temperature contrast. For our study, the most relevant are the lower tropospheric temperature and humidity profiles. By assimilating the vast amount of data, especially the satellite observations, such profiles in the ERA-Interim are consistently and reasonably accurate in the extrapolar regions. The good agreement between the observed and simulated monthly time series shown in Figure 3a corroborates this assessment. Biases in the reanalysis temperature and humidity profiles, if any, shall not be the leading causes in the CFC-11 retrievals here.
4. Biases and uncertainties in clear-sky detection: all our retrievals assume clear-sky measurements only. Thus, the clear-sky detection used in the actual observational data set is critically important to the retrievals. The cloud detection here is what has been done in the CERES SSF data set: it relies on the MODIS pixels within a CERES footprint, and each MODIS pixel has to pass a multistep threshold test for cloud detection (Trepte et al., 2019). Compared to more accurate cloud detection by space-borne LIDAR, its correct rate over the nonpolar region is estimated to be 90–96%. Since it is a threshold-based detection, it is always possible to misclassify some challenging footprints, e.g., a MODIS pixel with subvisible thin cirrus that has a small optical depth that cannot be detected. Moreover, a clear-sky footprint can still contain aerosols that absorb in the CFC-11 band, e.g., dust aerosols. But such an aerosol scenario is not considered by our LUT. We believe that such a thin cloud or absorptive aerosol contamination are the largest unknown factors in our retrieval and trend analysis. For example, the interannual variations of thin cloud scene statistics could affect our CFC-11 retrievals, contributing to the large year-to-year variation, as shown in Figures 6b–6d. The dust aerosols over the Arabian Peninsula, as well as other desert areas, can also affect the CFC-11 retrievals. Ideally, these factors can be remedied if we have good observations of thin clouds and aerosols that are absorptive in the mid-IR.

6. Conclusions and Discussion

This study investigates the feasibility of using current nadir-view satellite observations to estimate the CFC-11 surface concentration (with assumed uniform vertical distribution in the troposphere) and its long-term trend with near-global coverage. AIRS instrument has excellent radiometric calibration and stability, together with its dense sampling pattern, making it ideal for such long-term trend studies (e.g., Pan & Huang, 2018; Pan et al., 2015; Peterson et al., 2019). By carefully selecting two pairs of AIRS channels, the double difference in brightness temperatures, dΔBTs, can retain the CFC-11 absorption signals while largely cancel effects from other absorbers in the atmosphere. As a proof of the concept, we have shown that over the 11 sites of which ground measurements have been used in the previous CFC-11 studies, dΔBTs from the AIRS clear-sky observations and their trends agree well with their simulated counterparts based on the measured CFC-11 concentrations and ERA-Interim reanalysis temperature and humidity profiles. Using a LUT approach, we then retrieve monthly CFC-11 concentrations for each 30° by 10° grid between 55°N and 55°S over the entire 16 years (2003 to 2018). The trends of retrieved CFC-11 concentrations over the aforementioned 11 sites show larger uncertainties than the counterparts from actual ground observations. Nevertheless, all trends from the ground observations fall into the 95% confidence intervals of the retrieved trends. The linear trends between two periods (i.e., 2003–2018 vs. 2003–2012) show a statistically significant difference over the northern-hemispheric midlatitude zone, suggesting a slowdown of CFC-11 reduction after 2012. The spatial maps of CFC-11 trends over the same two periods show statistically significant contrast over the Shandong peninsula, which is consistent with the previous findings. Admittedly, the retrieval here is challenging and relies on multiple factors. We have examined such factors, and we conclude that the uncertainties associated with the clear-sky detection in the satellite data sets are likely the leading factors for the retrieval uncertainties. Though statistically significant contrast between the linear trends over the two periods are also seen in other places, no conclusive statement can be reached at this stage given such influential factors that affect the retrieval uncertainties and secular trends.

Although the CFC-11 absorption band is weak and overlaps with other greenhouse gas absorption bands, we show here that the signals can indeed be extracted from the observed nadir-view radiances. The dΔBT derived from AIRS observations is dominated by the CFC-11 variation. Though the accuracy of retrieved CFC-11 from such observed dΔBT can be hindered by multiple factors, such time series of dΔBT can still be valuable. For example, a chemical transport model can produce different synthetic dΔBTs based on different CFC-11 emission scenarios and reanalysis meteorological fields. Then such synthetic dΔBT time series can be compared with the observed ones to assess which emission scenario leads to a better agreement with the actual observations. Such "signal-to-radiance" approach avoids the complexity in the retrievals and can still provide meaningful assessment for different chemical transport model simulations. Moreover, the channels used here are also covered by other operational infrared nadir sounders such as Cross-track Infrared Sounder (CrIS; Han et al., 2013; Strow et al., 2013) on NASA Suomi-NPP and Infrared Atmospheric Sounding Interferometer (IASI; Hilton et al., 2012) on EUMESAT Metop satellite series. Both CrIS and IASI have demonstrated excellent calibration and stability, comparable to or even better than AIRS. Thus, it is possible to apply a similar method to extract CFC-11 signals from such satellite observations. Moreover, the successors of CrIS and IASI have been planned for the incoming decade. Therefore, this approach can potentially help provide a continuous way of monitoring CFC-11 from space without additional satellite planning and cost.

Data Availability Statement

The HATS combined CFC-11 measurements and description are available online (https://www.esrl.noaa.gov/gmd/hats/combined/CFC11.html). The WDCGG CFC-11 measurements are download online (https://gaw.kishou.go.jp/). The AIRS data were obtained online (http://airsl1.gesdisc.eosdis.nasa.gov/data/Aqua_AIRS_Level1/AIRIBRAD.005) and the CERES data online (https://asdc.larc.nasa.gov/project/CERES/CER_SSF_Aqua-FM3-MODIS_Edition4A). ECMWF ERA-Interim data are downloaded online (http://apps.ecmwf.int/datasets/data/interim-full-daily/). The CFC-11 retrievals and the LUTs used for retrievals are available online (https://zenodo.org/record/3786979#.X5cpXe0pA2w).

Acknowledgments

We wish to thank Dr. Luke Western and the other two anonymous reviewers for their constructive suggestions, which greatly improved the clarity and readability of this paper. This research is supported by NASA Terra/Aqua/Suomi-NPP program under grant 80NSSC18K1033 awarded to the University of Michigan with a subcontract to the University of Maryland at Baltimore County.

References

Anderson, G. P., Berk, A., Chetwynd, J. H., Harder, J., Fontenla, J. M., Shettle, E. P., et al. (2007). Using the MODTRAN™5 radiative transfer algorithm with NASA satellite data: AIRS and SORCE. *Proceedings of SPIE*, *6565*, 65651O. https://doi.org/10.1117/12.721184

Aumann, H. H., Broberg, S., Elliott, D., Gaiser, S., & Gregorich, D. (2006). Three years of AIRS radiometric calibration validation using sea surface temperatures. *Journal of Geophysical Research*, *111*, D16S90. https://doi.org/10.1029/2005JD006822

Aumann, H. H., Broberg, S., Manning, E., & Pagano, T. S. (2019). Radiometric stability validation of 17 years of AIRS data using sea surface temperatures. *Geophysical Research Letters*, *46*, 12,504–12,510. https://doi.org/10.1029/2019GL085098

Aumann, H. H., Chahine, M. T., Gautier, C., Goldberg, M. D., Kalnay, E., McMillin, L. M., et al. (2003). AIRS/AMSU/HSB on the aqua mission: Design, science objectives, data products, and processing systems. *IEEE Transactions on Geoscience and Remote Sensing*, *41*(2), 253–264. https://doi.org/10.1109/TGRS.2002.808356

Aumann, H. H., & Pagano, T. S. (2008). Using AIRS and IASI data to evaluate absolute radiometric accuracy and stability for climate applications. Paper presented at Conference on Atmospheric and Environmental Remote Sensing Data Processing and Utilization IV - Readiness for GEOSS II, Spie-Int Soc Optical Engineering, San Diego, CA. https://doi.org/10.1117/12.795225

Baldridge, A. M., Hook, S. J., Grove, C. I., & Rivera, G. (2009). The ASTER spectral library version 2.0. *Remote Sensing of Environment*, *113*(4), 711–715. https://doi.org/10.1016/j.rse.2008.11.007

Borbas, E. E., Hulley, G., Feltz, M., Knuteson, R., & Hook, S. (2018). The Combined ASTER MODIS Emissivity over Land (CAMEL) part 1: Methodology and high spectral resolution application. *Remote Sensing*, *10*(4), 643. https://doi.org/10.3390/rs10040643

Brown, A. T., Volk, C. M., Schoeberl, M. R., Boone, C. D., & Bernath, P. F. (2013). Stratospheric lifetimes of CFC-12, CCl4, CH4, CH3Cl and N2O from measurements made by the Atmospheric Chemistry Experiment-Fourier Transform Spectrometer (ACE-FTS). *Atmospheric Chemistry and Physics*, *13*(14), 6921–6950. https://doi.org/10.5194/acp-13-6921-2013

Chahine, M. T., Pagano, T. S., Aumann, H. H., Atlas, R., Bernet, C., Blaisdell, J., et al. (2006). AIRS: Improving weather forecasting and providing new data on greenhouse gases. *Bulletin of the American Meteorological Society*, *87*(7), 911–926. https://doi.org/10.1175/BAMS-87-7-911

Chen, X. H., & Huang, X. L. (2014). Usage of differential absorption method in the thermal IR: A case study of quick estimate of clear-sky column water vapor. *Journal of Quantitative Spectroscopy and Radiation Transfer*, *140*, 99–106. https://doi.org/10.1016/j.jqsrt.2014.02.019

Chen, X. H., Huang, X. L., Loeb, N. G., & Wei, H. L. (2013). Comparisons of clear-sky outgoing far-IR flux inferred from satellite observations and computed from three most recent reanalysis products. *Journal of Climate*, *26*(2), 478–494. https://doi.org/10.1175/JCLI-D-12-00212.1

Conway, T. J., Tans, P. P., Waterman, L. S., Thoning, K. W., Kitzis, D. R., Masarie, K. A., & Zhang, N. (1994). Evidence for interannual variability of the carbon cycle from the NOAMCMDL global air sampling network. *Journal of Geophysical Research*, *99*(D11), 22,831–22,855. https://doi.org/10.1029/94JD01951

Dee, D. P., Uppala, S. M., Simmons, A. J., Berrisford, P., Poli, P., Kobayashi, S., et al. (2011). The ERA-Interim reanalysis: Configuration and performance of the data assimilation system. *Quarterly Journal of the Royal Meteorological Society*, *137*(656), 553–597. https://doi.org/10.1002/qj.828

Feltz, M., Borbas, E., Knuteson, R., Hulley, G., & Hook, S. (2018). The Combined ASTER MODIS Emissivity over Land (CAMEL) part 2: Uncertainty and validation. *Remote Sensing*, *10*(5), 664. https://doi.org/10.3390/rs10050664

Han, Y., Revercomb, H., Cromp, M., Gu, D. G., Johnson, D., Mooney, D., et al. (2013). Suomi NPP CrIS measurements, sensor data record algorithm, calibration and validation activities, and record data quality. *Journal of Geophysical Research: Atmospheres*, *118*, 12,734–12,748. https://doi.org/10.1002/2013JD020344

Hilton, F., Armante, R., August, T., Barnet, C., Bouchard, A., Camy-Peyret, C., et al. (2012). Hyperspectral Earth observation from IASI: Five years of accomplishments. *Bulletin of the American Meteorological Society*, *93*(3), 347–370. https://doi.org/10.1175/BAMS-D-11-00027.1

Hoffmann, L., Kaufmann, M., Spang, R., Müller, R., Remedios, J. J., Moore, D. P., et al. (2008). Envisat MIPAS measurements of CFC-11: Retrieval, validation, and climatology. *Atmospheric Chemistry and Physics*, *8*(13), 3671–3688. https://doi.org/10.5194/acp-8-3671-2008

Huang, X. L., Chen, X. H., Potter, G. L., Oreopoulos, L., Cole, J. N. S., Lee, D. M., & Loeb, N. G. (2014). A global climatology of outgoing longwave spectral cloud radiative effect and associated effective cloud properties. *Journal of Climate*, *27*(19), 7475–7492. https://doi.org/10.1175/JCLI-D-13-00663.1

Huang, X. L., Chen, X. H., Zhou, D. K., & Liu, X. (2016). An observationally based global band-by-band surface emissivity dataset for climate and weather simulations. *Journal of the Atmospheric Sciences*, *73*(9), 3541–3555. https://doi.org/10.1175/jas-d-15-0355.1

Huang, X. L., Loeb, N. G., & Yang, W. Z. (2010). Spectrally resolved fluxes derived from collocated AIRS and CERES measurements and their application in model evaluation: 2. Cloudy sky and band-by-band cloud radiative forcing over the tropical oceans. *Journal of Geophysical Research*, *115*, D21101. https://doi.org/10.1029/2010JD013932

Huang, X. L., Yang, W. Z., Loeb, N. G., & Ramaswamy, V. (2008). Spectrally resolved fluxes derived from collocated AIRS and CERES measurements and their application in model evaluation: 1. Clear sky over the tropical oceans. *Journal of Geophysical Research*, *113*, D09110. https://doi.org/10.1029/2007JD009219

Hulley, G. C., Hook, S. J., Manning, E., Lee, S.-Y., & Fetzer, E. (2009). Validation of the Atmospheric Infrared Sounder (AIRS) version 5 land surface emissivity product over the Namib and Kalahari deserts. *Journal of Geophysical Research*, *114*, D19104. https://doi.org/10.1029/2009JD012351

Japan Meteorological Agency and World Meteorological Organization (2012). WMO WDCGG data summary No. 36, Tokyo. https://gaw.kishou.go.jp/static/publications/summary /sum36/sum36.pdf.

Lin, Y. J., Gong, D. C., Lv, S. J., Ding, Y. Z., Wu, G. C., Wang, H., et al. (2019). Observations of high levels of ozone-depleting CFC-11 at a remote mountain-top site in southern China. *Environmental Science & Technology Letters*, *6*(3), 114–118. https://doi.org/10.1021/acs.estlett.9b00022

Loveland, T., Reed, B., Brown, J., Ohlen, D., Zhu, Z., Yang, L., & Merchant, J. (2000). Development of a global land cover characteristics database and IGBP DISCover from 1 km AVHRR data. *International Journal of Remote Sensing*, *21*(6–7), 1303–1330. https://doi.org/10.1080/014311600210191

McClatchey, R., Fenn, R., Selby, J., Volz, F., & Garing, J. (1972). Optical properties of the atmosphere, Tech. Rep. AFCRL-72-0497, AFGL (OPI), Hanscom AFB, MA 01731.

Minnis, P., Sun-Mack, S., Young, D., Heck, P. W., Garber, D., & Chen, Y. (2011). CERES edition-2 cloud property retrievals using TRMM VIRS and Terra and Aqua MODIS data—part I: Algorithms. *IEEE Transactions on Geoscience and Remote Sensing*, *49*(11), 4374–4400. https://doi.org/10.1109/TGRS.2011.2144601

Minschwaner, K., Hoffmann, L., Brown, A., Riese, M., Müller, R., & Bernath, P. F. (2013). Stratospheric loss and atmospheric lifetimes of CFC-11 and CFC-12 derived from satellite observations. *Atmospheric Chemistry and Physics*, *13*(8), 4253–4263. https://doi.org/10.5194/acp-13-4253-2013

Montzka, S. A., Dutton, G. S., Yu, P., Ray, E., Portmann, R. W., Daniel, J. S., et al. (2018). An unexpected and persistent increase in global emissions of ozone depleting CFC-11. *Nature*, *557*(7705), 413–417. https://doi.org/10.1038/s41586-018-0106-2

Pagano, T. S., Aumann, H. H., Hagan, D. E., & Overoye, K. (2003). Prelaunch and in-flight radiometric calibration of the Atmospheric Infrared Sounder (AIRS). *IEEE Transactions on Geoscience and Remote Sensing*, *41*(2), 265–273. https://doi.org/10.1109/TGRS.2002.808324

Pan, F., & Huang, X. L. (2018). The spectral dimension of modeled relative humidity feedbacks in the CMIP5 experiments. *Journal of Climate*, *31*(24), 10,021–10,038. https://doi.org/10.1175/JCLI-D-17-0491.1

Pan, F., Huang, X. L., Guo, H., & Strow, L. L. (2015). Linear trends and closures of 10-year observations of AIRS stratospheric channels. *Journal of Climate*, *28*(22), 8939–8950. https://doi.org/10.1175/JCLI-D-15-0418

Peterson, C. A., Chen, X., Yue, Q., & Huang, X. (2019). The spectral dimension of Arctic outgoing longwave radiation and greenhouse efficiency trends from 2003 to 2016. *Journal of Geophysical Research: Atmospheres*, *124*, 8467–8480. https://doi.org/10.1029/2019JD030428

Prinn, R. G., Weiss, R. F., Arduini, J., Arnold, T., DeWitt, H. L., Fraser, P. J., et al. (2018). History of chemically and radiatively important atmospheric gases from the Advanced Global Atmospheric Gases Experiment (AGAGE). *Earth System Science Data*, *10*(2), 985–1018. https://doi.org/10.5194/essd-10-985-2018

Rigby, M., Park, S., Saito, T., Western, L. M., Redington, A. L., Fang, X., et al. (2019). Increase in CFC-11 emissions from eastern China based on atmospheric observations. *Nature*, *569*(7757), 546–550. https://doi.org/10.1038/s41586-019-1193-4

Rothman, L. S., Gordon, I. E., Barbe, A., Benner, D. C., Bernath, P. F., Birk, M., et al. (2009). The HITRAN 2008 molecular spectroscopic database. *Journal of Quantitative Spectroscopy and Radiation Transfer*, *110*(9–10), 533–572. https://doi.org/10.1016/j.jqsrt.2009.02.013

Simpson, I. J., Blake, D. R., Barletta, B., Meinardi, S., Blake, N. J., Wang, T., et al., (2019). Recent CFC-11 Enhancements in China, Nepal, Pakistan, Saudi Arabia and South Korea. Abstract A33T-2896, 2019 Fall AGU meeting, San Francisco, Dec 9-13, 2019.

Strow, L. L., & Hannon, S. E. (2008). A 4-year zonal climatology of lower tropospheric CO2 derived from ocean-only Atmospheric Infrared Sounder observations. *Journal of Geophysical Research*, *113*, D18302. https://doi.org/10.1029/2007JD009713

Strow, L. L., Hannon, S. E., Machado, S. D., Motteler, H. E., & Tobin, D. C. (2006). Validation of the Atmospheric Infrared Sounder radiative transfer algorithm. *Journal of Geophysical Research*, *111*, D09S06. https://doi.org/10.1029/2005JD006146

Strow, L. L., Motteler, H., Tobin, D., Revercomb, H., Hannon, S., Buijs, H., et al. (2013). Spectral calibration and validation of the Cross-track Infrared Sounder (CrIS) on the Suomi NPP satellite. *Journal of Geophysical Research: Atmospheres*, *118*, 12,486–12,496. https://doi.org/10.1002/2013JD020480

Trepte, Q. Z., Minnis, P., Sun-Mack, S., Yost, C. R., Chen, Y., Jin, Z., et al. (2019). Global cloud detection for CERES edition 4 using Terra and Aqua MODIS data. *IEEE Transactions on Geoscience and Remote Sensing*, *57*, 9410–9449. https://doi.org/10.1109/TGRS.2019.2926620

Western, L. M., Rougier, J. C., Watson, I. M., & Francis, P. N. (2020). Evaluating nonlinear maximum likelihood optimal estimation uncertainty in cloud and aerosol remote sensing. *Atmospheric Science Letters*, *21*(8).

World Meteorological Organization (WMO) (2011). *Scientific Assessment of Ozone Depletion: 2010* (p. 516). Geneva, Switzerland: Global Ozone Research and Monitoring Project—Report No. 52.